JOURNAL OF MATERIALS SCIENCE **36** (2001) 5739–5746

Nanostructure of atmospheric and high-pressure crystallised poly(ethylene-2,6-naphthalate)

M. C. GARCÍA GUTIÉRREZ, D. R. RUEDA, F. J. BALTÁ CALLEJA
Instituto de Estructura de la Materia, CSIC, Serrano 119, 28006 Madrid, Spain
E-mail: imtb421@iem.cfmac.csic.es

N. STRIBECK
Institut f. Technische und Makromolekulare Chemie, Universität Hamburg, Bundesstr. 45, 20146 Hamburg, Germany
E-mail: norbert@stribeck.desy.de

R. K. BAYER
Institut f. Werkstofftechnik, Universität GH Kassel, Mönchebergstr.3, 34109 Kassel, Germany

Poly(ethylene-2,6-naphthalate) (PEN) was crystallized from the glassy state at atmospheric pressure (beyond the end of primary crystallization) and from the melt at high pressure. The structure was characterized using small-angle X-ray scattering (SAXS), wide-angle X-ray scattering (WAXS), differential scanning calorimetry (DSC) and density measurements. The SAXS patterns were analysed using the interface distribution function (IDF) method. For the materials prepared at ambient pressure the crystallinity inside the layer stacks remains nearly constant during the secondary crystallization process. On the other hand, the volume filled with the stacks increases as a function of crystallization temperature (T_c) and time (t_c). For $T_c > 200°\text{C}$ secondary crystallisation goes along with a dynamic rearrangement of the primary stacks, as concluded from variations of the layer thickness distributions in the SAXS data. For $T_c < 200°\text{C}$ primary lamellae are stable, and both insertion of new crystal lamellae into existing stacks and generation of additional stacks is found. In contrast to PET, two different kinds of layer stacks are not observed in the PEN nano-composites. Materials prepared at 400 MPa exhibit high roughness of the crystalline domain surfaces. Depending on T_c there is a continuous transformation from the α to the β-crystal modification, but hardly any change of the long period. Crystal thickness increases, both at the expense of the amorphous thickness and of the volume filled with lamellar stacks. The structure of samples showing two melting peaks is discussed in terms of a dual lamellar contribution of correlated and uncorrelated nano-crystallites, respectively.

1. Introduction

Poly(ethylene-2,6-naphthalate) (PEN) is a polyester which is known for its superior physical properties as compared to the common poly(ethylene terephthalate) (PET). The high T_g value of PEN ($T_g \sim 120°\text{C}$) results in enhanced mechanical properties (elastic modulus, hardness, creep resistance, lower shrinkage, etc) [1, 2] and makes this polymer attractive for engineering purposes. Buchner *et al.* studied the structure development of PEN from the glass, and the influence of crystallization conditions on polymorphism using *in situ* WAXS and SAXS measurements [3]. The influence of crystallization and physical ageing on the properties of PEN, as well as the study of the emerging morphology, as revealed by electron microscopy have been reported [4–6]. Results on the melting behaviour and the microstructure, derived from X-ray scattering, of semicrystalline PEN prepared by cold crystallization have been reported recently also [7, 8].

It is well-known that in PET under common crystallisation conditions a spherulitic microstructure is generated [9, 10], whereas PEN only tends to form a dendritic structure, with considerable amounts of the material remaining amorphous [6]. In preceding studies we have examined the nanostructure of PET produced by high pressure crystallisation from the melt [11, 12]. It was found that in high pressure crystallized PET the relatively thick crystalline lamellae are separated by amorphous layers of extremely low thickness only.

The aim of the present study is to extend the above investigations to further examine the nanostructure of PEN developed after crystallization, both under atmospheric and high-pressure crystallisation conditions. Crystallisation at ambient pressure is a common commercial process. In particular when crystallising at elevated temperature, primary crystallisation is a fast process, whereas secondary crystallisation may take hours to finish. Therefore, it is of interest to examine the

0022–2461

morphological changes in the secondary crystallisation regime. The study of the structure-micromechanical property relationships will be the object of a separate publication.

2. Experimental

2.1. Materials

Samples were prepared from commercial PEN pellet material (Eastman PEN 14991) dried in vacuum at 116°C for 24 h. Two types of samples were prepared:

Samples crystallised at atmospheric pressure. Amorphous PEN films were obtained by melt pressing in vacuum for 2 min at 280°C and quenched in ice water. The amorphous samples were crystallised by placing them at various temperatures ($T_c = 165$, 180, 220 and 245°C). Crystallisation times ($t_c = 0.5, 2, 24$ h) for which primary crystallisation is completed (i.e. volume is filled with dendritic and other morphological structures) were chosen. Secondary crystallisation was interrupted at various times.

High pressure crystallised samples. 2 mm thick PEN platelets with a diameter of 20 mm were prepared in a hydraulic press. The material was molten in a cylindrical mould reaching the crystallisation temperature within 25 min. Thereafter the melt was pressed at 40 MPa for 5 min. The pressure was then increased up to 400 MPa. After a crystallisation time $t_c = 1$ h the temperature was decreased to 45°C within 10 min. Finally, the pressure was released to ambient condition.

2.2. Techniques

Wide-angle X-ray scattering (WAXS) was recorded on a Philips PW 1710 goniometer. In all scattering experiments nickel-filtered Cu K_α radiation was used. A volume crystallinity index from WAXS,

$$X_{cW} = \frac{\rho}{\rho_c} \frac{I_{cr}}{I_{tot}} \tag{1}$$

was computed from the area I_{tot} of the total scattering and the area I_{cr} of the crystalline peaks, determined after fitting the scattering curve of an amorphous sample to the amorphous halo of the semicrystalline samples. The fraction of β-modification crystallites, ϕ_β, was estimated by fitting a superposition of a pure α-modification pattern and a pure β-modification WAXS curve (from Ref. [3]) to the patterns of the high pressure crystallised samples.

SAXS measurements were carried out in a Kratky Compact Camera, equipped with proportional counter and energy discriminator. The integral length of the receiving slit was set to 2.01 nm^{-1} in reciprocal vector units, its magnitude, s, being defined by $(2/\lambda)\sin\theta$ (with λ being the wavelength of radiation and 2θ the scattering angle). Generally, calibration of the scattering intensity in absolute units was carried out [13]. However, for the high pressure crystallised material the sample thickness was non-uniform because the material was very brittle. Because sample thickness had to be estimated, the resulting absolute intensity represents only an approximation. Every scattering curve is composed of two overlapping parts, measured with different adjustments of the Kratky camera. The composite scattering curves cover the interval $0.01 \text{ nm}^{-1} < s < 1 \text{ nm}^{-1}$.

Density was measured using a density gradient column containing a mixture of CCl_4 and n-hexane. Volume crystallinity from density,

$$X_{c\rho} = \frac{\rho - \rho_a}{\rho_c - \rho_a} \tag{2}$$

was computed using the measured density value of an amorphous sample, $\rho_a = 1330.4$ kg/m^3, the reported [3] densities of the two crystalline modifications $\rho_c^\alpha = 1407$ kg/m^3, $\rho_c^\beta = 1439$ kg/m^3 and the fraction of the β-modification, ϕ_β, using the equation $\rho_c = \rho_c^\beta \phi_\beta + \rho_c^\alpha (1 - \phi_\beta)$

Differential scanning calorimetry (DSC) measurements were carried out in a Perkin-Elmer DSC 7. The volume crystallinity from calorimetry,

$$X_{cDSC} = \frac{\rho}{\rho_c} \frac{\Delta H_f}{\Delta H_f^o}, \tag{3}$$

was determined using a value of $\Delta H_f^o = 120$ J/g for the heat of fusion of the fully crystalline state.

3. Data evaluation

The general method of data evaluation applying the interface distribution function (IDF) analysis has been extensively discussed in previous papers [14–16]. Therefore, here only a summarised overview is presented in Appendix I. Raw scattering curves from the Kratky camera were corrected for background scattering and calibrated in absolute units. The region in which Porod's law is valid was then searched and the quantities which describe the deviations of the observed two-phase system from an ideal one were determined resulting in a slit-smeared interference function $\tilde{G}_{id}(s)$. This function was, thereafter transformed into the one-dimensional IDF, $g_1(x)$, of the lamellar two-phase system, which contains the topological information of the two-phase system and can easily be fitted by a unified statistical model comprising both paracrystalline stacking and lattice models [15–17]. In the case of the high pressure samples, the shape of $g_1(x)$ indicates a considerable surface roughness of the crystalline domains. Thus roughness had to be considered by adding a specific term to the model function. The fitting parameters were: a weight W; the average thickness of amorphous and crystalline layers, l_a, and l_c; their relative widths, σ_a / l_a and σ_c / l_c and a parameter σ_H taking into account skewness of the layer thickness distributions. The extended model has two additional parameters, namely the weight W_r and the width σ_r of a Gaussian roughness distribution.

4. Results and discussion

4.1. Crystallisation at atmospheric pressure

4.1.1. Wide angle X-ray scattering

The WAXS patterns from all samples crystallised at atmospheric pressure are shown in Fig. 1. The patterns show that the crystalline phase corresponds to the pure α-modification. Thus crystallinity from density, $X_{c\rho}$, was computed from the density values of the α-modification crystallites ($\rho_c^\alpha = 1407$ kg/m^3) and the

TABLE I Volume crystallinity values as determined from density, $X_{c\rho}$, and from WAXS, X_{cW}, for atmospheric pressure crystallised PEN

T_c (°C)	t_c (h)	$X_{c\rho}$	X_{cW}
165	2	0.24	0.22
	24	0.25	0.22
180	0.5	0.25	0.21
	2	0.27	0.21
	24	0.29	0.22
220	0.5	0.33	0.24
	2	0.37	0.30
	24	0.38	0.28
245	0.5	0.38	0.26
	2	0.41	0.27
	24	0.44	0.32

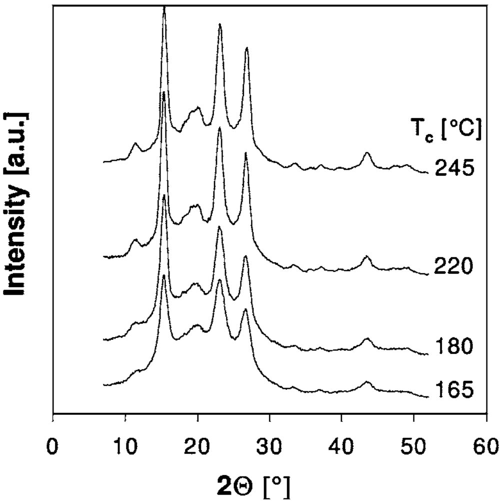

Figure 1 WAXS patterns of different PEN samples crystallised at atmospheric pressure for 24 h at different temperatures.

density of the amorphous phase ($\rho_a = 1330.4$ kg/m^3) [3]. The crystallinity values obtained are given in Table I as a function of crystallization temperature.

4.1.2. Small angle X-ray scattering

Fig. 2 shows the variation of the scattering curve as a function of crystallisation time. Here it is seen a shift of the SAXS maximum towards higher scattering angles. Fig. 3 shows the corresponding trend as a function of crystallisation temperature. A scattering maximum (long period) can clearly be identified in each one of the curves. As crystallisation time, t_c, increases, the scattering maximum shifts towards higher scattering angles. In contrast, the scattering peak moves towards smaller angles with increasing crystallisation temperature (Fig. 3). The determined non-topological parameters of the two-phase system are presented in Table II. One immediately sees that the invariant increases not only with increasing crystallisation temperature, but also with rising crystallisation time. The thickness of the transition zone, t_i decreases, both, with increasing crystallisation time and temperature.

After having determined the non-topological parameters, we have analysed the two-phase topology by computing the interface distribution function (IDF) in physical space from the scattering curves. Figs 4 and 5 illustrate the IDF computed from the scattering curves. The curves have been fitted by the statistical model described in Appendix I [15–17]. The structural parameters (morphology) determined by the fit are presented in Table III. Assignment of the thicknesses to crystalline and amorphous phases, respectively, follows from the following considerations:

TABLE II Atmospheric pressure crystallised PEN

T_c (°C)	t_c (h)	$\tilde{I}_{Fl}/V$ (e.u./nm^4)	t_i (nm)	$\tilde{A}_P$ (e.u./nm^7)	Q (e.u./nm^6)	l_p (nm)
165	2	450	1.4	1.2	144	3.0
	24	550	1.4	1.5	178	3.1
180	0.5	520	1.4	1.2	170	3.8
	3	530	0.9	1.3	184	3.7
	24	450	1.2	1.3	177	3.6
220	0.5	470	1.4	0.9	175	5.0
	3	470	1.5	1.0	191	4.8
	24	500	1.1	1.3	227	4.6
245	0.5	450	1.2	0.9	189	5.5
	3	510	1.1	0.9	235	6.3
	24	450	1.0	1.1	228	5.2

Non-topological structural parameters as determined from the isotropic SAXS as a function of crystallisation time and temperature.

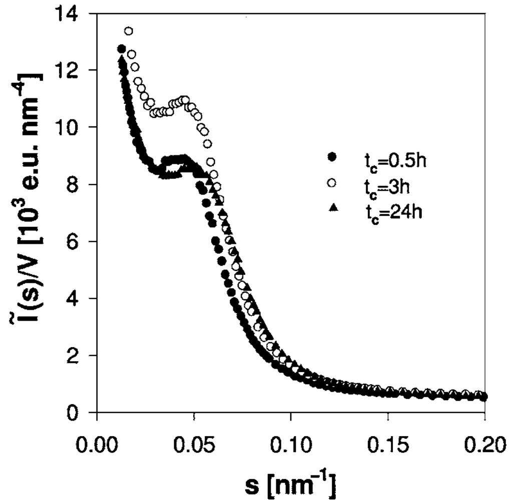

Figure 2 Absolute slit-smeared SAXS intensity $\tilde{I}(s)/V$ of PEN crystallised at ambient pressure and 245°C for different t_c values (indicated in the plot).

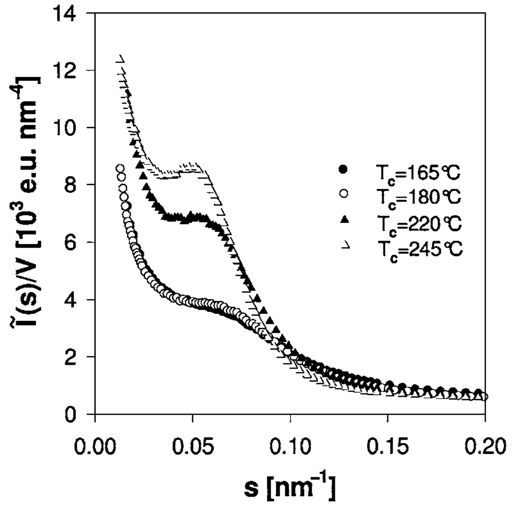

Figure 3 SAXS curves of PEN crystallised at ambient pressure for 24 h as a function of T_c (indicated in the plot).

The volume crystallinity of a semicrystalline polymer can be expressed in terms of three factors [18],

TABLE III Atmospheric pressure crystallised PEN

T_c (°C)	t_c (h)	l_1 (nm)	l_2 (nm)	$(\sigma_1/l_1)_{obs}$	$(\sigma_2/l_2)_{obs}$	L (nm)
165	2	4.6	3.0	0.63 ± 0.01	0.55 ± 0.01	7.6
	24	4.4	3.0	0.64 ± 0.02	0.50 ± 0.01	7.4
	0.5	5.3	3.0	0.64 ± 0.04	0.53 ± 0.04	8.3
180	3	4.5	3.3	0.69 ± 0.01	0.54 ± 0.01	7.8
	24	4.9	2.8	0.51 ± 0.02	0.50 ± 0.02	7.7
220	0.5	6.6	4.2	0.48 ± 0.03	0.48 ± 0.03	10.8
	3	7.6	4.0	0.41 ± 0.02	0.44 ± 0.02	11.6
	24	6.9	4.3	0.39 ± 0.03	0.39 ± 0.03	11.2
245	0.5	8.5	5.9	0.37 ± 0.01	0.32 ± 0.01	14.4
	3	8.0	5.5	0.35 ± 0.01	0.42 ± 0.02	13.5
	24	7.1	5.6	0.37 ± 0.03	0.31 ± 0.02	12.7

Layer stack structural parameters determined from SAXS data as a function of crystallisation time and temperature. l_1, l_2: average layer thicknesses (am., cryst.). $(\sigma_1/l_1)_{obs}$, $(\sigma_2/l_2)_{obs}$: relative widths of the layer thickness distributions. Long period $L = l_1 + l_2$. If no error is specified, the error is in the order of the magnitude of the last digit.

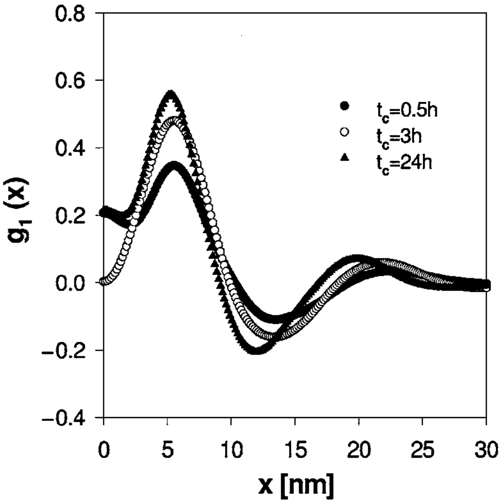

Figure 4 Interface distribution function (IDF) computed from the scattering intensities of Fig. 2 describe the topology of the stacks from crystalline and amorphous layers. Samples crystallised at $T_c = 245°C$ for different t_c values.

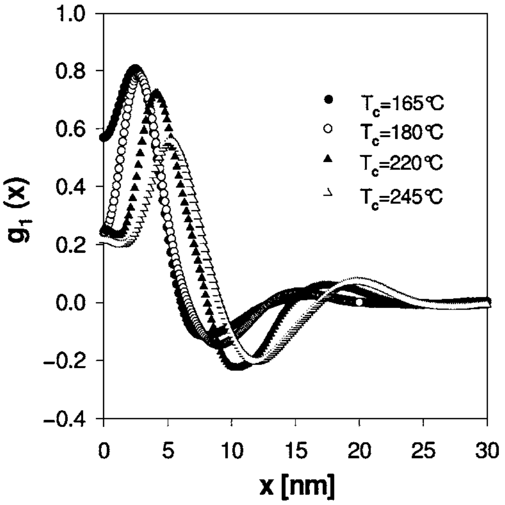

Figure 5 Interface distribution function computed from the scattering intensities shown in Fig. 3. Samples crystallised at different t_c.

which may vary independently during the process of crystallisation,

$$X_c = X_s X_L X_{cL} \tag{4}$$

where X_s is the volume fraction of spherulites within the sample, X_L is the fraction occupied by lamellar stacks inside the spherulite volumes, and X_{cL} is the crystallinity within the lamellar stacks called "linear crystallinity". The X_{cL} value is determined from the SAXS parameters l_1 and l_2. During primary crystallisation the volume fraction of spherulites, X_S increases from 0 to 1. After primary crystallisation is completed, $X_S = 1$ and only secondary crystallisation proceeds further. Hence,

$$X_c = X_L X_{cL} \tag{5}$$

applies. It is thus obvious that linear crystallinity always has to be greater or equal to the average volume crystallinity and that the crystallinity values determined from WAXS and density can be considered only as a lower limit for the linear crystallinity. Consequently the average layer thickness parameter l_1 in Table III must be attributed to the crystalline layers and linear crystallinity has to be computed from $X_{cL} = l_1/(l_1 + l_2)$. Since we assume that primary crystallisation is completed for all the samples of Table II, Equation 5 applies and X_L can be computed. Using the crystallinity values $X_{c\rho}$ the results presented in Table IV are obtained. The data reveal that inside the layer stacks all the samples show an almost constant crystallinity, X_{cL}, of about 60% with a statistical deviation of 4%. On the other hand, the volume filled by layer stacks, X_L, is increasing as a function both of increasing crystallisation temperature and time. For secondary crystallisation two different models are discussed in the literature (see Fig. 6). According to the insertion model [19, 20] crystal layers are inserted into the amorphous gaps of existing lamellar stacks. According to the two-stack model [21]

TABLE IV PEN crystallised at atmospheric pressure with varying crystallisation temperature and time

T_c [°C]		165			180	
t_c[h]	2		24	0.5	3	24
X_{cL}	0.61		0.59	0.64	0.58	0.63
X_L	0.41		0.44	0.41	0.48	0.48
T_c [°C]		220			245	
t_c [h]	0.5	3	24	0.5	3	24
X_{cL}	0.61	0.66	0.61	0.59	0.59	0.56
X_L	0.56	0.58	0.64	0.668	0.71	0.80

Linear crystallinity inside the layer stacks, X_{cL}, and volume fraction of the stacks, X_L, as determined using the total crystallinity, $X_{c\rho}$, and the topological structure parameters from SAXS.

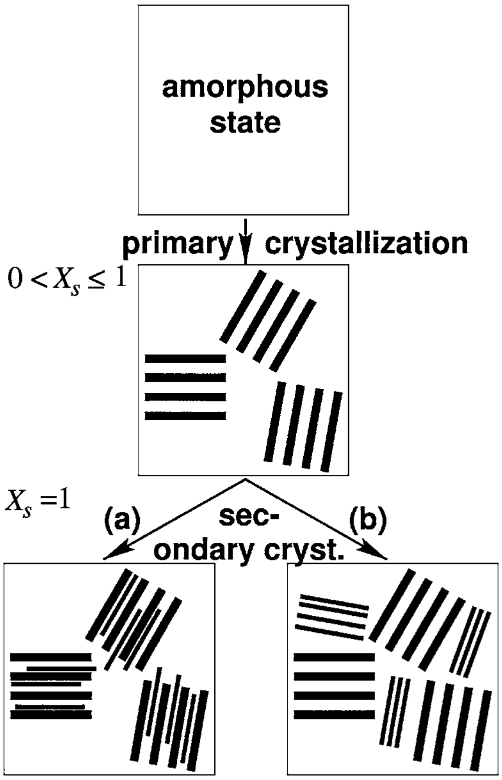

Figure 6 Secondary crystallisation models for polymers. (a) Insertion model; (b) Two–stack model.

complete secondary layer stacks emerge within large amorphous regions. Both models resort to the notion that crystalline lamellae formed during primary crystallisation can be considered relatively stable and that secondary crystal layers can be discriminated from the primary ones. Hence, if primary layers are stable, secondary crystallisation must at least cause broadening of the crystalline layer thickness distribution (Table III; $(\sigma_1/l_1)_{\mathrm{obs}}$). Such an effect is observed at the lower crystallisation temperatures. But with samples crystallised at temperatures above 200°C the distribution of crystallite thicknesses becomes narrower as secondary crystallization develops. This finding indicates that at high crystallisation temperature dynamic rearrangement of primary crystalline lamellae takes place. Alternative notions related to considerable changes in crystallite perfection can be ruled out because of the fact that changes observed in the invariant

$$Q = X_{\mathrm{L}} X_{\mathrm{cL}} (1 - X_{\mathrm{cL}}) \Delta\rho_{\mathrm{el}}^2 \qquad (6)$$

are only moderate (with $\Delta\rho_{\mathrm{el}}$ designating the electron density difference between amorphous and crystalline phase). Thus only with the samples crystallised at lower temperatures it appears reasonable to attempt to distinguish between the above mentioned two classical models of secondary crystallisation. Table III shows that the long period L decreases with decreasing T_{c}. Moreover, one would expect a considerable multi-stack morphology to become visible in the IDF. All in all, data appear to favour, both, the insertion model and the generation of complete new secondary stacks which, in the case of PEN, cannot be distinguished from the primary ones. The latter conclusion is drawn from the observed increase of X_{L} as a function of crystallisation time.

4.2. Crystallization at high pressure

4.2.1. Density

The crystallinity index from WAXS, X_{cW}, the fraction of β-modification crystals, ϕ_β, the density ρ, the volume fraction crystallinity from density, $X_{\mathrm{c}\rho}$ and the volume crystallinity from calorimetry, X_{cDSC} values of PEN crystallised under high pressure are collected in Table V for various crystallisation temperatures T_{c}.

4.2.2. Wide angle X-ray scattering

WAXS scans of PEN samples crystallised at high pressure are presented in Fig. 7. The scattering curves show that all high-pressure crystallised samples contain considerable amounts of amorphous material. Thus the crystallinity values of high-pressure crystallised PEN are considerably lower than those of the *"nanocrystalline"* PET from our previous study [11, 12] crystallised under similar conditions. The curves exhibit a gradual transition from almost pure α-modification when crystallised at 300°C to almost pure β-modification in the sample crystallised at 340°C (cf. Table V).

4.2.3. Small angle X-ray scattering

Fig. 8 shows the slit-smeared SAXS curves in absolute units. Only estimates of the sample thicknesses are possible. Hence the absolute intensity values are approximate values as well. A small angle peak is observed at $s \sim 0.7\ \mathrm{nm}^{-1}$ for all high pressure crystallised samples. Fig. 9 shows both the IDFs computed from the scattering curves and the fits using the statistical model with a roughness term as described in Appendix I. It is obvious that the correlation among the layers decays

TABLE V PEN crystallised under high pressure for 1 h at different temperatures

T_{c} (°C)	300	320	330	340
X_{cW}	0.42	0.43	0.53	0.43
ϕ_β	0.06	0.17	0.35	0.93
$\rho(\mathrm{kg/m^3})$	1374.7	1379.7	1387.3	1390.1
$X_{\mathrm{c}\rho}$	0.57	0.61	0.65	0.56
X_{cDSC}	0.54	0.60	0.63	0.54

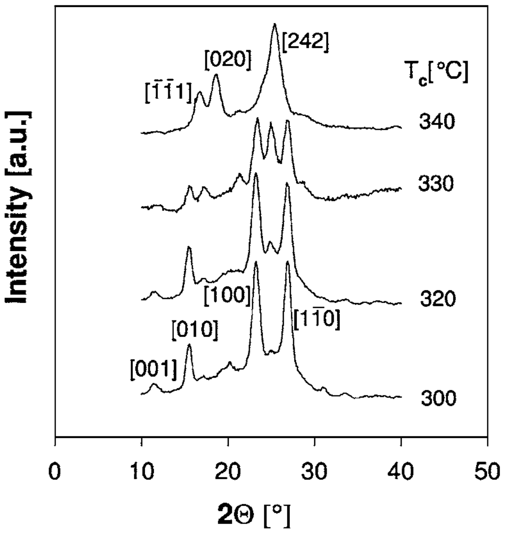

Figure 7 WAXS diffractograms of PEN crystallised under high pressure for 1 h at different T_{c}.

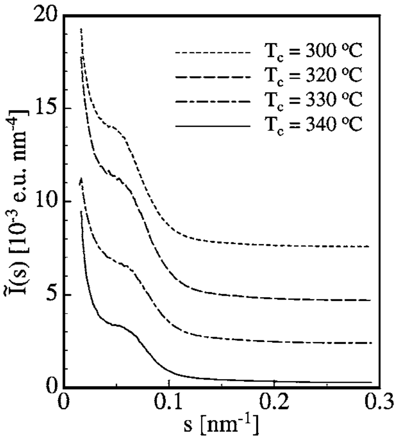

Figure 8 Slit-smeared SAXS curves for high-pressure crystallised PEN as a function of T_c. The curves are stacked for the reason of clarity.

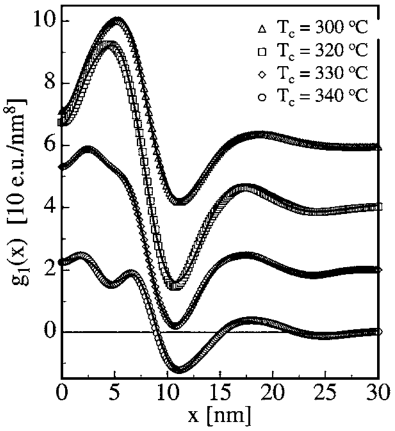

Figure 9 IDFs from PEN samples crystallised at high pressure at different T_c. Symbols indicate the curves computed from the scattering curves in Fig. 8. Underlying solid lines show fits using one-dimensional layer stack statistics.

within a short range of 25 nm for all samples. Thus the lamellar stacks contain a few layers only. The long period, estimated from the first minimum of the curves, does not change significantly as a function of T_c. On the other hand, the separation between the thickness distribution of the amorphous layers and that of the crystalline ones obviously becomes better with increasing T_c. This observation may either be caused from a change of crystallinity or from a narrowing of the layer thickness distributions. An answer to the question comes from the model fits presented in Table VI. The obtained fits confirm the fact that the long period $L = l_a + l_c$ does not change as a function of T_c. However, there is an increase of l_c at the expense of l_a, leading to a considerable narrowing of the corresponding layer thickness distribution. As a consequence, the crystallinity within the stacks, $X_{cL} = l_c/(l_a + l_c)$, exhibits an increase, whereas $X_L = X_c/X_{cL}$, decreases as a function of increasing T_c. The conspicuous finding of non-crystallisable material outside the layer stacks agrees with previous electron microscopic observations showing that outside the dendritic structure of the PEN there are regions, which are incapable of crystallising [6].

Application of a model function without a roughness term (cf. Appendix I) only is possible for the samples crystallised at 330°C and at 340°C. However, even in this case the quality of the fit is low. Comparison of the results from both kinds of fits indicates that not considering the roughness primarily leads to changes in the parameters of the amorphous layer thickness distribution and to a decrease in the average layer thickness and to a broadening in its distribution as a whole.

TABLE VI High-pressure crystallised PEN as a function of T_c

T_c (°C)	l_a (nm)	l_c (nm)	$(\sigma_a/l_a)_{obs}$	$(\sigma_c/l_c)_{obs}$	X_{cL}	ϕ_L
300	4.4	6.7	0.61 ± 0.03	0.29 ± 0.01	0.60	0.95
320	3.6	7.2	0.67 ± 0.05	0.29 ± 0.02	0.67	0.91
330	3.1	7.2	0.69 ± 0.02	0.27 ± 0.02	0.70	0.93
340	3.9	7.5	0.63 ± 0.04	0.20 ± 0.03	0.66	0.85

Parameters describing the layer thickness distributions from model fits on the SAXS data and computed crystallinities. l_a, l_c: average thickness of the amorphous and the crystalline layers, respectively. $(\sigma_a/l_a)_{obs}$, $(\sigma_c/l_c)_{obs}$: apparent relative widths of the layer thickness distributions. X_{cL} volume crystallinity inside the layer stacks. ϕ_L volume fraction filled with layer stacks. If no error is specified, the error is in the order of the magnitude of the last digit.

In contrast to PET [11], high pressure crystallised PEN does not present two different kinds of layer stacks. The SAXS exhibits only one single component of lamellar stacks, the linear crystallinity of which is high, but nevertheless remains in the semicrystalline regime. In contrast to this finding, the predominant component of thicker layer crystal stacks from high pressure crystallised PET revealed thin nanocrystalline layer stacks, i.e. amorphous layers of ~1.3 nm thickness alternating with ~10 nm crystalline layers. In addition 5–10% of the sample volume was filled with a second, semicrystalline component.

In contrast to the WAXS results on the PEN samples, no indication of the two crystal modifications are found in the SAXS data. The reason for this is the distorted short-range order arrangement of the layers leading to rather diffuse scattering data.

4.2.4. Differential scanning calorimetry observations

Typical thermograms of the high pressure crystallised PEN samples are shown in Fig. 10. The samples

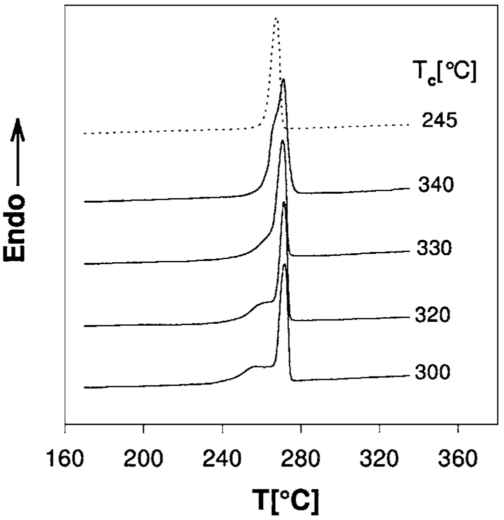

Figure 10 DSC thermograms of PEN crystallised for 1 h at high pressure (400 MPa) and different temperatures (solid lines) as compared to PEN crystallised at ambient pressure (dotted line).

crystallised at lower temperature clearly exhibit a dual melting peak. The SAXS data, in turn, do not show any second layer stack component in the IDF. Thus the question arises, how this second DSC component can be described in terms of the semicrystalline structure. A hint is given from the absolute values of the SAXS background scattering. At the two lower crystallisation temperatures the estimated fluctuation background is twice as large as the background found at high crystallisation temperature. Although the values are only rough estimates because of the approximated sample thicknesses values, the observed effect is significant. Thus we may identify the low melting component with an ensemble of uncorrelated thin crystallites, which in the SAXS pattern only lead to an increased density fluctuation level by peaking out from their amorphous environment. Nevertheless, these nanosize crystallites contribute to the crystallinities X_{cDSC} and $X_{c\rho}$ determined from DSC and density, whereas WAXS crystallinity is smaller, because it does not recognize small imperfect crystallites (cf. Table V).

5. Conclusions

Both, atmospheric pressure and high pressure crystallised PEN yield peculiar nanostructures which differ considerably from the ones found for PET. Nevertheless, PEN reveals as well an imperfect nanostructure exhibiting a short-range correlation only. Thus the statistical nature of the structure with varying "lattice constants" and layer thicknesses must be considered during the evaluation of SAXS data in order to gain meaningful structural parameters. In particular, the high pressure material requires thorough analysis, because of the exceptional high level of roughness found at the surface of its crystallites. Elaborate data analysis and results from other methods like WAXS, DSC and density determination result in a better understanding of the nanosize structure as a function of materials processing. In short, the peculiar crystallisation process of PEN appears to be governed by sparse volume filling during primary crystallisation. Thereafter, during the following secondary crystallisation the remaining amorphous volume is gradually filled by secondary stacks, which show the same structure as the primary ones. At low crystallisation temperatures there are additional indications for crystallite insertion into the existing stacks. At high crystallisation temperatures a dynamic rearrangement of the primary stacks during the secondary process is observed.

Acknowledgements

Grateful acknowledgement is due to the MCYT, Spain, Grant BFM2000-1474 for the support of this work.

Appendix I: Quantitative data evaluation of the SAXS curves

After subtraction of the blind scattering curve multiplied by the measured sample absorption factor, the intensity $\tilde{I}(s)/V$ is transformed to an interference function, $\tilde{G}_{id}(s)$ of the ideal two-phase system:

$$\tilde{G}_{id}(s) = \frac{(\tilde{I}(s)/V - \tilde{I}_{Fl}/V)s^3}{F(t_i, s)} - \tilde{A}_P \tag{7}$$

with

$$F(t_i, s) = \left(1 - 8\left(\frac{\pi t_i s}{3}\right)^2 \mathrm{erfc}\left(\frac{2\pi t_i s}{3}\right)\right) + 4\sqrt{\frac{\pi t_i s}{3}}\exp\left(-4\left(\frac{\pi t_i s}{3}\right)^2\right). \tag{8}$$

In this function, deviations according to the non-ideal nature of the multiphase system are eliminated by consideration of a constant fluctuation background, $\tilde{I}_{Fl}/V$, as well as a width of the transition zone, t_i, at the interface between the crystalline and the amorphous layer. The determination of $\tilde{I}_{Fl}/V$ is carried out on the plot of $ln(s^3(\tilde{I}(s)/V - \tilde{I}_{Fl}/V))$ vs. $s^{1.81}$ as proposed by Koberstein, Morra and Stein [22]. The criterion for choosing the value of $\tilde{I}_{Fl}/V$ is the linearisation of the observed Porod-slope in this plot over the longest possible interval. An estimation for t_i is gained from the slope of the straight line and of $\tilde{A}_P$ from the extrapolated intercept with the vertical axis. Both values are fine-tuned in a plot of $\tilde{G}_{id}(s)$ using the postulate that the interference function must vanish in the Porod regime. An even more detailed description of the procedure has been reported reported [14].

In addition, it is now possible to compute the slit-smeared scattering curve $\tilde{I}_{id}(s)$ of the ideal two-phase system from $\tilde{G}_{id}(s)$. Moreover, because $\tilde{A}_P$ governs the asymptotic shape of the intensity for large scattering angles, the integral scattering intensity over reciprocal space (invariant Q) can be determined with high accuracy. The invariant can, then, be expressed in terms of crystallinity and density contrast between amorphous and crystalline phases (cf. Equation 3). Another basic parameter of the two-phase system, the average chord length l_p, is proportional to the ratio $Q/\tilde{A}_P$.

The integral of the interference function should vanish if the crystalline and amorphous layers were smooth. If, on the other hand, some surface roughness is present, the integral becomes negative. The surface roughness and the layer thickness distributions become apparent in the interface distribution function [23], $g_1(x)$, which is proportional to the second derivative of the one-dimensional correlation function [24] and can be computed from $\tilde{G}_{id}(s)$ by a Fourier–Bessel transformation

$$g_1(x) = \pi \int_o^\infty \tilde{G}_{id}(s)(4\mathrm{J}_o(2\pi xs) - 2[2\pi xs + (1/2\pi xs)]\,\mathrm{J}_1(2\pi xs))\,\mathrm{d}s. \tag{9}$$

Here the surface roughness shows up in a peak centred at $x = 0$. Remaining is the information on the statistical arrangement of crystalline and amorphous layers within the lamellar stack, distinguished by an infinite series of distance distributions, $h_i(x)$. If an assumption is made on the principal statistics of layers within the stack, only the first two distance distributions, $h_1(x)$ and $h_2(x)$, can freely be chosen. These two functions describe the thickness statistics of the amorphous lamellae within the layer stacks and the corresponding statistics associated to the crystalline lamellae.

For some of the samples examined in the present study we found a considerable overlap of the roughness distribution $h_r(x)$ and the thickness distribution $h_1(x)$. The general method of fitting statistical models to the interface distribution functions has been described previously in detail [15]. With reference to the older method we have now added an additional Gaussian function to the topological model in order to be able to separate $h_r(x)$. The new term is a function of two parameters, namely a weight W_r modelling the strength of the roughness distribution and a width parameter σ_r. One should bear in mind that these roughness parameters, $\tilde{I}_{Fl}/V$ and t_i are, in general, strongly correlated with each other. The study of this problem has been the object of a recent report [25].

Again, the topological model contributes with six structural parameters: A weight W, the average layer thicknesses l_1 and l_2, the width parameters σ_1/l_1 and σ_2/l_2 and finally a parameter controlling the skewness of the layer thickness distributions, σ_H. The relationship among the width parameters is controlled by a Mellin-convolution, and thus the observable standard deviation, $(\sigma_k/l_j)_{obs}$ is related to the model parameters according to

$$\left((\sigma_k/l_k)^2_{obs} + 1\right) = \left((\sigma_k/l_k)^2 + 1\right)\left(\sigma_H^2 + 1\right) \qquad (10)$$

The identification of the distributions as crystalline or amorphous has to be made from additional information.

References

1. A. M. GHAHEM and R. S. PORTER, *J. Polym. Sci. Polym. Phys. Ed.* **17** (1989) 480.
2. C. SANTA CRUZ, F. J. BALTÁ CALLEJA, H. G. ZACHMANN and D. CHEN, *J. Mater. Sci.* **27** (1992) 2161.
3. S. BUCHNER, D. WISWE and H. G. ZACHMANN, *Polymer* **30** (1989) 480.
4. D. R. RUEDA, A. VIKSNE, L. MALERS, F.J. BALTÁ CALLEJA and H. G. ZACHMANN, *Macromol. Chem. & Phys.* **195** (1994) 3869.
5. D. R. RUEDA, A. VARKALIS, A. VIKSNE, F. J. BALTÁ CALLEJA and H. G. ZACHMANN, *J. Polym. Sci., Polym. Phys. Ed.* **33** (1995) 1653.
6. F. J. BALTÁ CALLEJA, D. R. RUEDA, G. H. MICHLER and I. NAUMANN, *J. Macromol. Sci., Phys.* **B37** (1998) 411.
7. Z. DENCHEV, A. NOGALES, T. A. EZQUERRA, J. FERNANDES-NASCIMENTO and F. J. BALTÁ CALLEJA, *J. Polym. Sci., Polym. Phys. Ed.* **38** (2000) 1167.
8. Z. DENCHEV, A. NOGALES, I. SICS, T. A. EZQUERRA and F. J. BALTÁ CALLEJA, *ibid.* **39** (2001) 881.
9. H. G. ZACHMANN and H. A. STUART, *Makromol. Chem.* **41** (1960) 131.
10. G. GROENINCKX, H. REYNAERS, H. BERGHMANS and G. SMETS, *J. Polym. Sci., Polym. Phys. Ed.* **18** (19980) 1311.
11. N. STRIBECK, H. G. ZACHMANN, R. K. BAYER and F. J. BALTÁ CALLEJA, *J. Mater. Sci.* **32** (1997) 1639.
12. U. KÖNCKE, H. G. ZACHMANN and F. J. BALTÁ CALLEJA, *Macromolecules* **29** (1996) 6019.
13. S. POLIZZI, N. STRIBECK, H. G. ZACHMANN and R. BORDEIANU, *Colloid Polym. Sci.* **267** (1989) 281.
14. C. SANTA CRUZ, N. STRIBECK, H. G. ZACHMANN and F. J. BALTÁ CALLEJA, *Macromolecules* **24** (1991) 5980.
15. N. STRIBECK, *Colloid Polym. Sci.* **271** (1993) 1007.
16. N. STRIBECK, R. G. ALAMO, L. MANDELKERN and H. G. ZACHMANN, *Macromolecules* **28** (1995) 5029.
17. N. STRIBECK, *J. Phys. IV* **3** (1993) 507.
18. H. G. ZACHMANN and C. WUTZ, in "Crystallization of Polymers," edited by M. Dosiére (Kluwer Academic Publishers, 1993) p. 403.
19. J. WANG, M. ALVAREZ, W. ZHANG, Z. WU, Y. LI and B. CHU, *Macromolecules* **25** (1992) 6943.
20. B. S. HSIAO, K. H. GARDNER, D. Q. WU and B. CHU, *Polymer* **34** (1993) 3996.
21. D. C. BASSETT, R. H. OLLEY and I. A. M. AL RAHEIL, *ibid.* **29** (1988) 1745.
22. J. T. KOBERSTEIN, B. MORRA and R. S. STEIN, *J. Appl. Cryst.* **13** (1980) 34.
23. W. RULAND, *Colloid Polym. Sci.* **255** (1977) 417.
24. C. G. VONK and G. KORTLEVE, *Kolloid-Z. Z. Polymere* **220** (1967) 19.
25. N. STRIBECK, *J. Appl. Cryst.* **34** (2001) 496.

Received 1 June
and accepted 20 August 2001